

On the follow-up efforts of long-period transiting planet candidates detected with Gaia astrometry

A. Sozzetti,¹* P. Giacobbe,¹ M. G. Lattanzi,¹ and M. Pinamonti¹

¹INAF - Osservatorio Astrofisico di Torino, Via Osservatorio 20, I-10025 Pino Torinese, Italy

Accepted XXX. Received YYY; in original form ZZZ

ABSTRACT

The class of transiting cold Jupiters, orbiting at $\gtrsim 0.5\text{--}1.0$ au, is to-date underpopulated. Probing their atmospheric composition and physical characteristics is particularly valuable, as it allows for direct comparisons with the Solar System giant planets. We investigate some aspects of the synergy between Gaia astrometry and other ground-based and space-borne programs for detection and characterization of such companions. We carry out numerical simulations of Gaia observations of systems with one cold transiting gas giant, using Jovian planets around a sample of nearby low-mass stars as proxies. Using state-of-the-art orbit fitting tools, we gauge the potential of Gaia astrometry to predict the time of transit centre T_c for the purpose of follow-up observations to verify that the companions are indeed transiting. Typical uncertainties on T_c will be on the order of a few months, reduced to several weeks for high astrometric signal-to-noise ratios and periods shorter than ~ 3 yr. We develop a framework for the combined analysis of Gaia astrometry and radial-velocity data from representative ground-based campaigns and show that combined orbital fits would allow to significantly reduce the transit windows to be searched for, down to about ± 2 weeks ($2 - \sigma$ level) in the most favourable cases. These results are achievable with a moderate investment of observing time (~ 0.5 nights per candidate, ~ 50 nights for the top 100 candidates), reinforcing the notion that Gaia astrometric detections of potentially transiting cold giant planets, starting with Data Release 4, will constitute a valuable sample worthy of synergistic follow-up efforts with a variety of techniques.

Key words: astrometry – techniques: radial velocities – exoplanets – stars: low-mass – methods: numerical – methods: data analysis

1 INTRODUCTION

The class of long-period transiting giant planets, with orbital periods exceeding 1 yr, was first unveiled by the Kepler mission [Borucki et al. \(2010\)](#). These objects are cold, with equilibrium temperatures $T_{\text{eq}} \sim 200$ K. They constitute a valuable sample for comparative studies of their atmospheric composition and physical properties with those of the outer planets of our Solar System. However, the combination of low geometric transit probability and low signal-to-noise ratio (S/N) of the events (due to their limited number) has thus far translated in a few tens of long-period systems identified in the full Kepler dataset based on two- or single-transit events (e.g., [Wang et al. 2015](#); [Uehara et al. 2016](#); [Foreman-Mackey et al. 2016](#); [Beichman et al. 2018](#); [Herman et al. 2019](#)). The comprehensive analysis of available data from the K2 mission has more recently allowed to uncover a large sample of mono-transit candidates (e.g., [Osborn et al. 2016](#); [LaCourse & Jacobs 2018](#)), some of which, with estimated durations of tens of hours, might indeed correspond to new detections of long-period gas giants beyond the snow line (one such instance being the case of EPIC248847494b reported by [Giles et al. \(2018\)](#)). More will come, with over 1000 single-transit candidates

expected to be found by the TESS mission ([Villanueva et al. 2019](#); [Kunimoto et al. 2022](#)) and other significant numbers likely to be provided by the PLATO mission.

Long-period gas giants producing single-transit events warrant follow-up efforts for accurate period and mass determination, in order to down-select the optimal target sample for atmospheric characterization with e.g. JWST ([Beichman et al. 2014](#)). Archival searches and carefully-planned photometric monitoring programs from the ground ([Cooke et al. 2018](#); [Kovacs 2019](#); [Dholakia et al. 2020](#); [Yao et al. 2019, 2021](#)) and in space ([Cooke et al. 2019, 2020](#)) and ground-based radial-velocity (RV) work (e.g., [Hébrard et al. 2019](#); [Gill et al. 2020](#); [Dalba et al. 2020, 2021a,b, 2022](#); [Ulmer-Moll et al. 2022](#)) are typically the channels used for the purpose. However, space-based high-precision astrometry with the Gaia mission ([Gaia Collaboration et al. 2016, 2022b](#)) also bears the potential for important contributions to this task. On the one hand, depending on target magnitude and distance, Gaia will provide useful mass upper limits or actual astrometric detections of long-period transiting planets, particularly in the regime of orbital separations 1 – 4 au, for which Gaia achieves maximum sensitivity (e.g., [Lattanzi et al. 2000](#); [Casertano et al. 2008](#); [Sozzetti et al. 2014](#); [Perryman et al. 2014](#)). Indeed, [Holl et al. \(2022\)](#) report close to edge-on orbital solutions for a small sample of transiting systems identified by the Kepler and TESS mission, likely

* E-mail: alessandro.sozzetti@inaf.it

corresponding to the correct identification of the transits as low-mass stars based on Gaia DR3 astrometry. On the other hand, Gaia might in fact be seen itself as a target provider for photometric and spectroscopic follow-up observations. Recent studies indicate that Gaia has the potential to identify astrometrically hundreds of giant-planet systems with $P \geq 1$ yr having orbital inclinations compatible with a transit configuration (Sozzetti et al. 2014), some of which might be actually transiting (Perryman et al. 2014). In the sample of ~ 1900 candidate substellar companions presented in Gaia Collaboration et al. (2022a), 49 have orbital solutions with an inclination angle in the range [89,91] deg, i.e. compatible with a perfectly edge-on orbit, and the median period of these solutions is ~ 1.3 yr. The population of potentially edge-on systems is likely underestimated, given Gaia’s reduced sensitivity to such configurations extensively discussed in Gaia Collaboration et al. (2022a).

In this paper we investigate some aspects of the potential synergy between Gaia astrometry, Doppler measurements, and space-borne photometric time-series for improved characterization of long-period transiting giant-planet systems. We focus our attention on the problem of combining Gaia astrometry and follow-up radial-velocity time-series for improved forecast of the time of transit center, in order to identify the preferred regime of orbital separations that might effectively be probed by space-based photometric observations with CHEOPS, TESS, and PLATO. For this task we utilize as reference sample the Lépine & Gaidos (2011) all-sky catalog of bright, nearby M dwarfs, that maximizes the likelihood of high-precision orbit and mass determination with Gaia. All the findings described in this work can readily be scaled to other stellar and companion masses, and ranges of distance from the Sun. In Section 2 we describe the adopted setup of the Gaia simulations, while in Section 3 we present the details of our analysis tools. The main results are presented in Section 4, followed by a brief summary and discussion.

2 SIMULATION SCHEME

2.1 Gaia astrometry

The simulation of Gaia observations follows closely the observational scenario described in Sozzetti et al. (2014). Here we summarize and describe the main features of the setup:

1) The actual list of targets is based on the 8793 dM dwarf stars (in the approximate range $0.09 - 0.6 M_{\odot}$) from the *All-sky Catalog of Bright M Dwarfs* (Lépine & Gaidos 2011). As already noted in the Introduction, the choice of this catalogue was driven by our interest to choose a statistically significant, representative sample of relatively bright, nearby stars that would maximize detection efficiency (see Fig. 4 of Sozzetti et al. 2014). A coordinate-based cross-match between the Lépine & Gaidos (2011) catalogue, the Starhorse catalogue (Anders et al. 2022) and the Gaia DR3 archive returned a total of 5378 sources within ~ 100 pc from the Sun and with masses $\lesssim 0.70 M_{\odot}$. We did not investigate in detail the reasons behind the unmatched sources, as our intention is not to update the Lépine & Gaidos (2011) catalogue, but rather select a representative sample of well-classified sources for our purposes, and the sample size returned through the cross-match exercise was deemed satisfactory. In the four panels of Fig. 1 we show the distributions (dashed histograms) in G mag, distance d primary mass M_{\star} , and number N_{obs} of Gaia field transits (individual along-scan measurements w) for our sample (a consequence of the adopted scanning law, see e.g. Gaia Collaboration et al. 2016 for details), which are those appropriate for the adopted 5-yr mission duration. The sample has median values of stellar mass,

distance and magnitude are $\mathbf{M}[M_{\star}] \simeq 0.58 M_{\odot}$, $\mathbf{M}[d] \simeq 42$ pc, and $\mathbf{M}[G] \simeq 11.9$, respectively. The solid histograms of Fig. 1 correspond to the distributions of the same parameters for the sub-sample with statistically significant orbital semi-major axis derived in the astrometry-only fits (see Sec. 4.1). The only noticeable differences are typically slightly smaller primary masses ($\mathbf{M}[M_{\star}] \simeq 0.55 M_{\odot}$) and slightly shorter distances ($\mathbf{M}[d] \simeq 39$ pc), which is entirely expected given the scaling of the astrometric signature with M_{\star} and d .

2) The five standard astrometric parameters for each star in the sample (right ascension α , declination δ , the two proper motion components μ_{α} and μ_{δ} , and the parallax ϖ) were taken from the Gaia DR3 archive. The generation of planetary systems proceeded as follows. One planet was generated around each star (assumed not to be orbited by a stellar companion), with mass $M_p = 1M_J$; orbital periods were uniformly distributed in the range $0.2 \leq P \leq 5$ yr and eccentricities were distributed as a Beta function, following Kipping (2013); the orbital semi-major axis a_p was determined using Kepler’s third law; the inclination i of the orbits was fixed to 90 deg, while the two remaining angles, argument of periastron ω and longitude of the ascending node Ω , were uniformly distributed in the ranges $0 \leq \omega \leq 360$ deg and $0 \leq \Omega \leq 180$ deg, respectively; the epoch of periastron passage was uniformly distributed in the range $0 \leq T_0 \leq P$. The resulting astrometric signature induced on the primary was calculated using the standard formula corresponding to the semi-major axis of the orbit of the primary around the barycentre of the system scaled by the distance to the observer: $a_{\star} = (M_p/M_{\star}) \times (a_p/d)$. With a_p in au, d in pc, and M_p and M_{\star} in M_{\odot} , then a_{\star} is evaluated in arcsec.

3) As in Sozzetti et al. (2014), the error model adopts the established magnitude-dependent behavior of the along-scan formal uncertainties σ_w at the single-transit level in Gaia astrometry, with no additional contributions from unmodeled systematics (see e.g., Lindegren et al. 2021, red curve in Fig. A.1). The median of the CCD-level single-measurement uncertainties is $\sim 57 \mu\text{as}$, with a corresponding average σ_w three times lower¹. Given the typical magnitude of the Gaia positional uncertainties involved in the simulations, the astrometric ‘jitter’ induced by spot distributions on the stellar surface of active dwarf stars (e.g., Sozzetti 2005; Eriksson & Lindegren 2007; Makarov et al. 2009; Barnes et al. 2011; Sowmya et al. 2021; Meunier et al. 2020; Meunier & Lagrange 2022) was considered to be negligible, and therefore not included in the error model.

2.2 Radial velocities

Synthetic RV datasets were produced for all cases in which the Gaia astrometric orbit has its semi-major axis determined with good statistical significance, i.e. $a_{\star}/\sigma_a \geq 5$. For all datasets for which the astrometric orbit reconstruction satisfies the above criterion, we simulate RV campaigns with time-series of 20 data points uniformly distributed over three observing seasons. With typical 6-months intervals between successive seasons, each RV follow-up campaign lasts about 2.5 yr. Uncertainties are drawn from a Gaussian distribution with standard deviation of 10 m s^{-1} , which is appropriate for a typical integration time of 900 sec with average observing conditions on an early- to mid-M dwarf with $V \simeq 14$ mag (corresponding to $G \simeq 12$ mag at the peak of the distribution of Fig. 1) at a 4-m class telescope equipped with a HARPS/HARPS-N-like

¹ we recall a full Gaia transit corresponds to 9 consecutive CCD crossings on the astrometric focal plane of the satellite

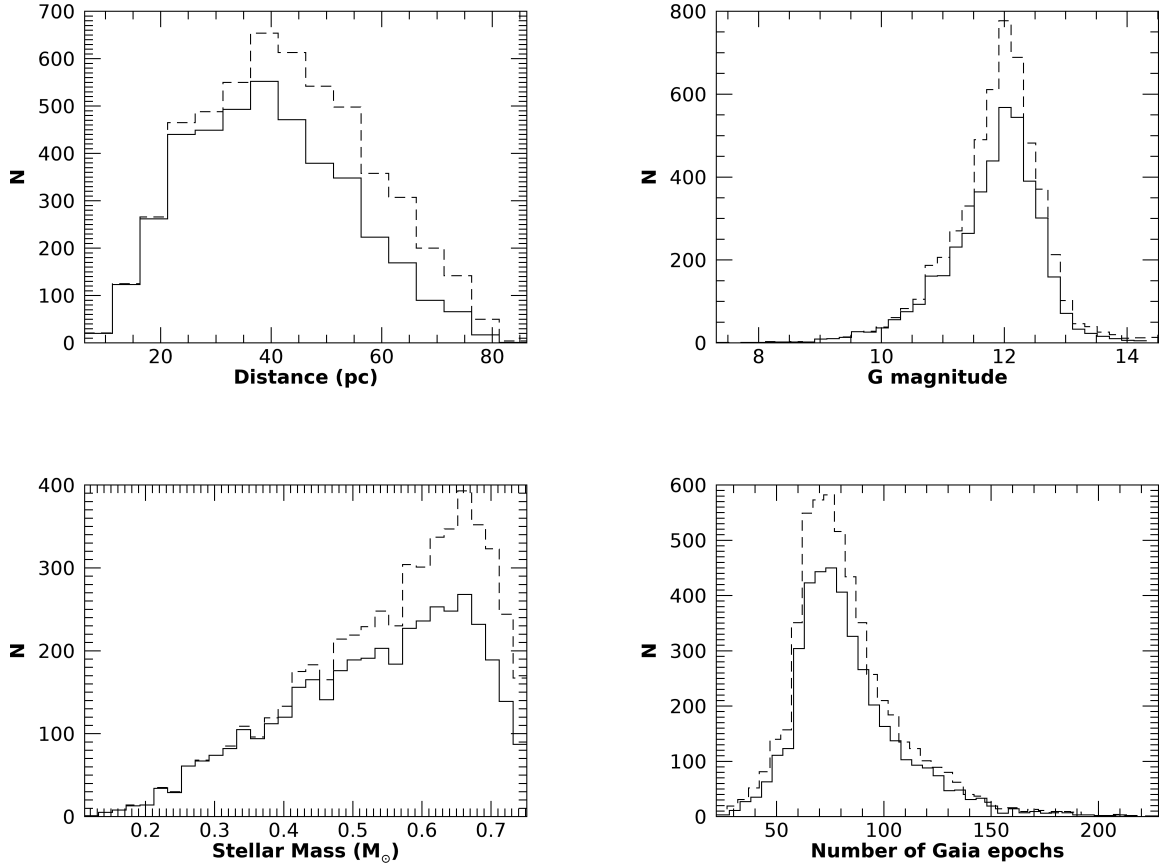


Figure 1. Top left: distance distribution of the M-dwarf sub-sample of the [Lépine & Gaidos \(2011\)](#) successfully cross-matched to Gaia DR3. Top right: The corresponding magnitude distribution at *G* band. Bottom left: the derived distribution of primary masses. Bottom right: number of individual Gaia field transits for the same sample. See text for additional details.

spectrograph. These numbers are illustrative and are not necessarily optimized having in mind for example the maximization of the number of targets for follow-up within a specific amount of observing time at any given observing facility. We stress that the illustrative example of a follow-up RV campaign is designed solely to provide a sense of the amount of observing time required for refinement of the orbit of the potentially transiting gas giant at intermediate separation identified by Gaia astrometry. The rather different problem of an RV campaign that also aims at exploring, for example, the existence of low-mass companions interior to the outer massive planet is left for future work.

3 MODELS AND ORBIT FITTING ALGORITHMS

The astrometry-only model (see e.g., [Holl et al. 2022](#) for details) adopts the following description for the time-series of one-dimensional along-scan coordinates:

$$w^{(\text{model})} = (\alpha + \mu_{\alpha} t) \sin \psi + (\delta + \mu_{\delta} t) \cos \psi + \varpi f_{\varpi} + (B X + G Y) \sin \psi + (A X + F Y) \cos \psi. \quad (1)$$

In Eq. 1 f_{ϖ} and ψ are the along-scan parallax factor and scan angle at time t , respectively, A , B , F , and G are four of the six Thiele-Innes coefficients (e.g., [Holl et al. 2022](#)) and are functions of a_{\star} , i , ω and Ω , while the elliptical rectangular coordinates X and Y are functions of P , T_0 and e .

The combined astrometry + RV model specifically implements the representation described in [Wright & Howard \(2009\)](#), in which:

$$w^{(\text{model})} = (\alpha + \mu_{\alpha} t) \sin \psi + (\delta + \mu_{\delta} t) \cos \psi + \varpi f_{\varpi} + H S + C T \quad (2)$$

$$RV^{(\text{model})} = \lambda H \cos \nu - \lambda C \sin \nu + V_0 = c \sin \nu + h \sin \nu + V_0. \quad (3)$$

In this case, H and C are the two remaining Thiele-Innes coefficients, ν is the true anomaly, and V_0 is the zero-point of the RV time-series (no provision is made to fit for long-term RV trends) while $\lambda(\varpi, P, e)$, $S(i, \Omega, X, Y, \psi)$ and $T(i, \Omega, X, Y, \psi)$ are defined as in Eqs. 67 and 74 of [Wright & Howard \(2009\)](#). This manipulation allows to adjust a common set of linear parameters to both astrometric and RV datasets, at the expense of now treating i , Ω and ϖ as three additional non-linear parameters.

Orbit fitting of Gaia astrometry only and Gaia astrometry + RVs is performed using a hybrid implementation of a Bayesian analysis based on the differential evolution Markov chain Monte Carlo (DE-MCMC) method ([Ter Braak 2006](#); [Eastman et al. 2013](#)). The final likelihood functions used in the DE-MCMC analysis are:

$$-\ln(\mathcal{L}^{\text{ast}}) = \frac{1}{2} \sum_{j=1}^{N_{\text{ast}}} \frac{(w_j^{(\text{obs})} - w_j^{(\text{model})})^2}{\sigma_{w,j}^2 + \sigma_{\text{jit,ast}}^2} + \frac{1}{2} \sum_{j=1}^{N_{\text{ast}}} \ln(\sigma_{w,j}^2 + \sigma_{\text{jit,ast}}^2) \quad (4)$$

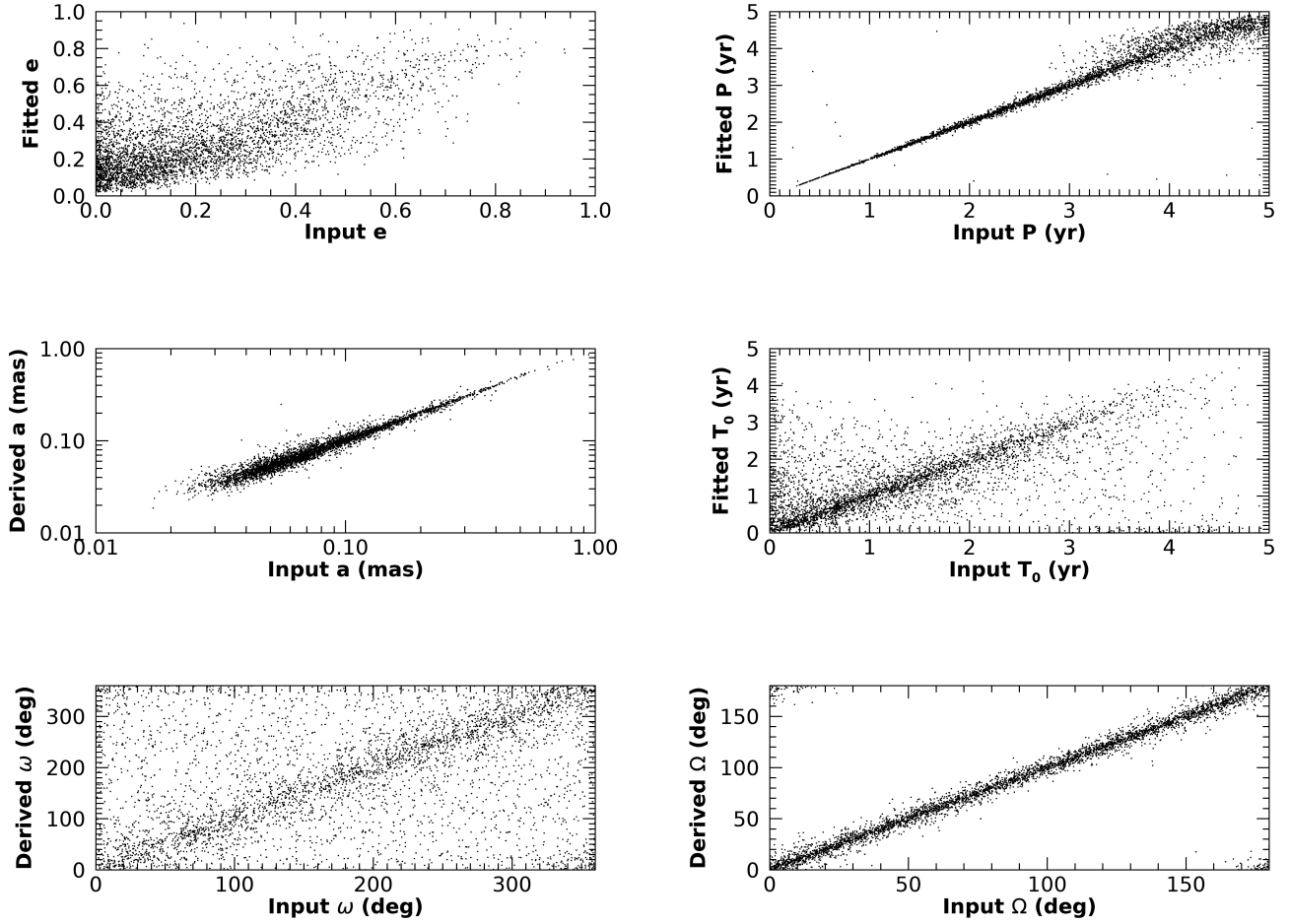


Figure 2. Fitted vs input value for orbital parameters in the astrometry-only solutions: Top left: eccentricity; top right: orbital period; center left: semi-major axis; center right: epoch of periastron; bottom left: argument of periastron; bottom right: longitude of the ascending node.

and

$$\begin{aligned}
 -\ln(\mathcal{L}^{\text{ast+RV}}) &= \frac{1}{2} \sum_{j=1}^{N_{\text{ast}}} \frac{\left(w_j^{(\text{obs})} - w_j^{(\text{model})}\right)^2}{\sigma_{w,j}^2 + \sigma_{\text{jit,ast}}^2} + \\
 &\quad \frac{1}{2} \sum_{j=1}^{N_{\text{ast}}} \ln\left(\sigma_{w,j}^2 + \sigma_{\text{jit,w}}^2\right) + \\
 &\quad \frac{1}{2} \sum_{j=1}^{N_{\text{RV}}} \frac{\left(RV_j^{(\text{obs})} - RV_j^{(\text{model})}\right)^2}{\sigma_{RV,j}^2 + \sigma_{\text{jit,RV}}^2} + \\
 &\quad \frac{1}{2} \sum_{j=1}^{N_{\text{RV}}} \ln\left(\sigma_{RV,j}^2 + \sigma_{\text{jit,RV}}^2\right) \quad (5)
 \end{aligned}$$

for the astrometry-only and astrometry+RV case, respectively. Uniform priors are used for the non-linear parameters adjusted the DEMCMC way, the exact ranges being $[0.0, 5.0]$ yr, $[0, P]$, $[0.0, 1.0]$, $[0, \pi]$, $[0, \pi]$ for P , T_0 , e , i , and Ω , respectively. We fit for uncorrelated jitter terms in both astrometry and RVs, which are added in quadrature to the formal uncertainties of the data, although no additional variations are included in either dataset, therefore the fitted values of $\sigma_{\text{jit,w}}$ and $\sigma_{\text{jit,RV}}$ are always in practice returned very close to zero, and will not be discussed further. We refer the reader to [Drimmel et al. \(2021\)](#) and [Holl et al. \(2022\)](#) for more details on the algo-

rithm. Following [Holl et al. \(2022\)](#), symmetric estimates of the 1σ formal uncertainties on the model parameters were obtained by reconstructing the covariance matrix directly from the Jacobians of all parameters for all observations. Standard conversion formulae (e.g., [Wright & Howard 2009](#); [Halbwachs et al. 2022](#)) are used to compute the Campbell elements (a_\star , ω , and Ω and i , for the astrometry-only solutions, a_\star and i for the astrometry+RV solutions) back from the Thiele-Innes parameters, and the corresponding formal uncertainties derived using linear error propagation.

4 RESULTS

4.1 Astrometry only: quality of orbit determination

We focus our analysis on the sub-sample of 4050 astrometric orbits (75% of the full sample) with $a_\star/\sigma_a \geq 5$ for which we also performed the combination with RVs. The six panels of Figure 2 show the overall agreement between fitted or derived orbital parameters and the 'truth'. One clearly identifies a number of expected features. For example, orbital periods are accurately recovered, with only a minor loss of accuracy as P approaches the nominal mission duration. Orbital eccentricity is more difficult to determine accurately, primarily due to the perfectly edge-on orbits (with consequent loss of information on the actual orbit shape), but with a second well-known effect of increasing difficulty to measure accurately values of $e \approx 0.0$.

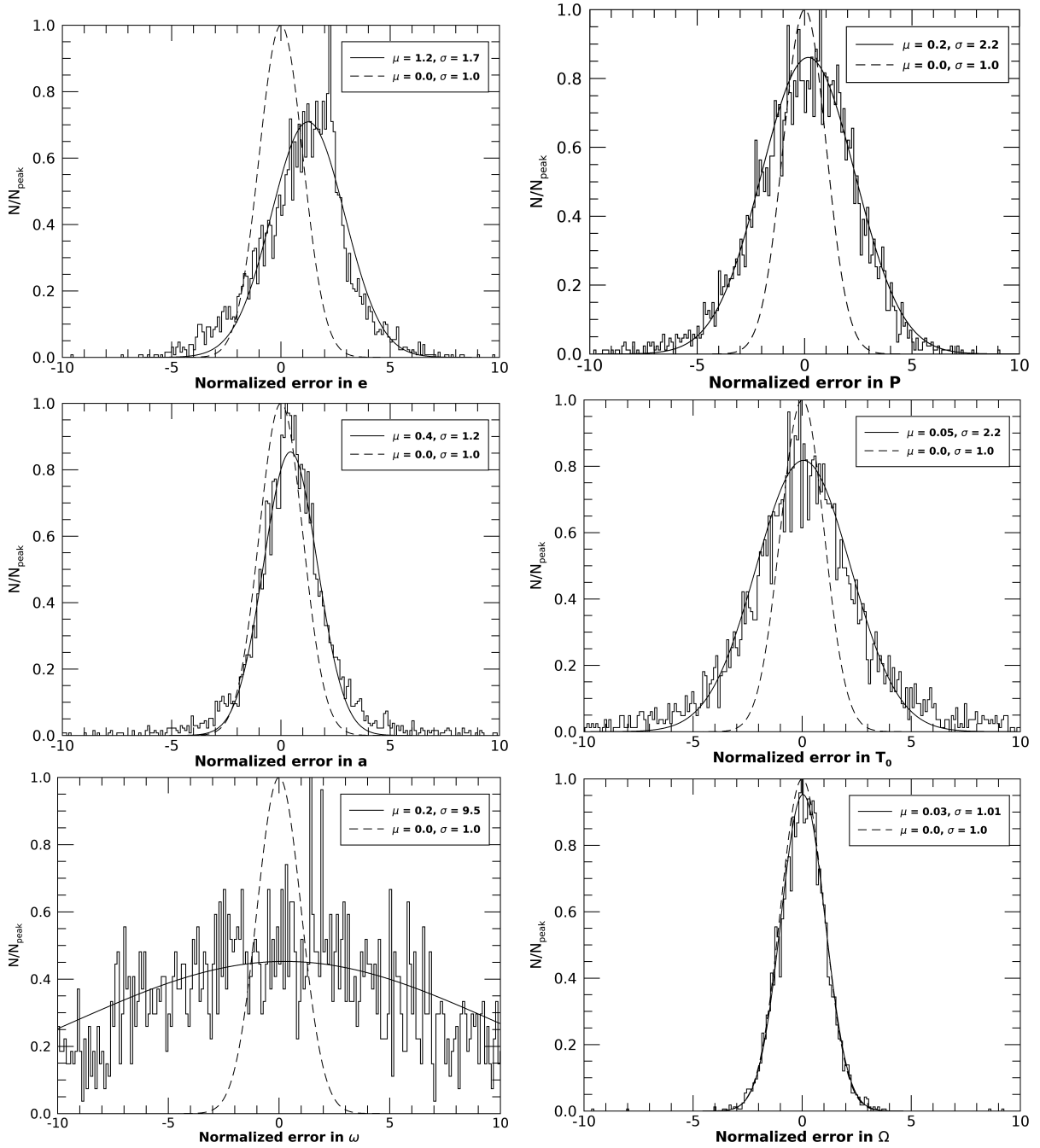


Figure 3. Distributions of normalized errors in the astrometry-only solutions (solid histograms). The ordering of the panels is the same as in Fig. 2. The solid lines correspond to a Gaussian fit of given mean μ and standard deviation σ . The dashed lines are Gaussians of zero mean and unit dispersion.

The two closely related parameters T_0 and ω are consequently also determined with significant spread around the 1:1 correlation lines. The longitude of the ascending node is instead very well determined, while we notice a mild systematic trend of recovery of overestimated values of the angular size of the perturbation, particularly for $a \lesssim 0.1$ mas. This can again be understood due to the combined effect of the edge-on configuration and the small orbit size compared to the magnitude of the individual measurement errors.

We can glean complementary insight on the quality of orbit reconstruction in our simulations using as proxy the precision with which the various orbital parameters are retrieved as a result of the orbit fitting procedure. The distribution of the ratio of the differences

between the fitted and true values of a parameter divided by their estimated uncertainties (from the covariance matrix of the solution or linear propagation), which we dub here normalized errors, should be distributed normally with zero mean and unit dispersion in case the latter correctly map the former (see e.g. Casertano et al. 2008; Holl et al. 2022). Distortions in the distribution inform on departures from this assumption due to e.g. biases in orbit reconstruction. The six panels of Fig. 3 show the distributions of normalized errors for the same parameters of Fig. 2. The central values of the distributions for Ω , ω , T_0 and P closely match the expectations. Larger positive biases for the normalized error distributions of a and especially e are present, as a further confirmation of the tendency to overestimate the

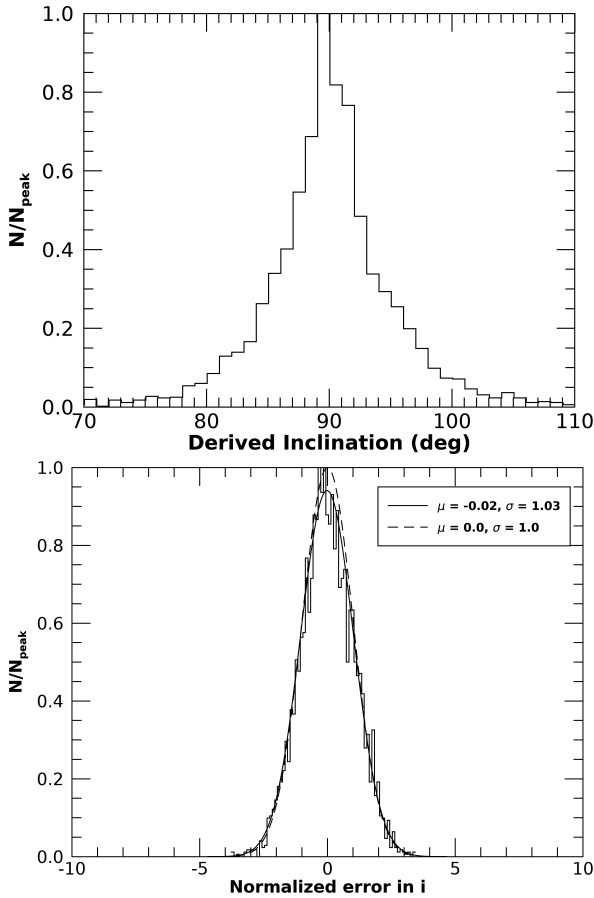


Figure 4. Top: Distribution of the derived values of orbital inclination in the astrometry-only solutions. Bottom: normalized errors in i . Histograms and lines have the same meaning as in Fig. 2 and 3.

values of the two parameters. For Ω and a the width of the distribution is in excellent agreement with the expectations. For e , P , T_0 and ω the departure from unit dispersion gets increasingly larger, an effect understood in terms of the biases discussed for Fig. 2 for the different parameters. As formal uncertainties from the covariance matrix of the solution tend to underestimate the true errors in a significant fraction of the cases, adopting the more standard approach of evaluating the ± 34.13 per cent intervals from the posterior distributions should be the preferred choice. Finally, we show in the two panels of Fig. 4 the histogram of derived inclination angles (keeping in mind the exact $i = 90^\circ$ simulated configuration) and the corresponding normalized error distribution. The median and standard deviation of the derived inclination distribution are $89.9^\circ \pm 4.5^\circ$, and 93% of the orbits have i determined to within 10 deg of a perfectly edge-on configuration. As for Ω , the formal uncertainties on i are found to be a very close representation of the true errors on the parameter.

We next focus our attention on aspects of the quality of the determination of the orbital parameters directly affecting the forecast for the time of transit center, i.e. P , T_0 , e , and ω (see next Section). We discuss in particular how their fractional errors (e.g., $\sigma_P = (P_{\text{fitted}} - P_{\text{true}})/P_{\text{true}}$, etc.) depend on the input values of the parameters and on the astrometric signal-to-noise ratio, defined as either $S/N_{\text{ast},1} = a_\star/\sigma_w$ (Casertano et al. 2008) or $S/N_{\text{ast},2} = (a_\star/\sigma_w) \cdot \sqrt{N_{\text{obs}}}$ (Sahlmann et al. 2015). The four panels of Fig. 5 show how the fractional error on σ_P , σ_{T_0} , σ_e , and σ_ω varies as a function of the value of the input parameters themselves.

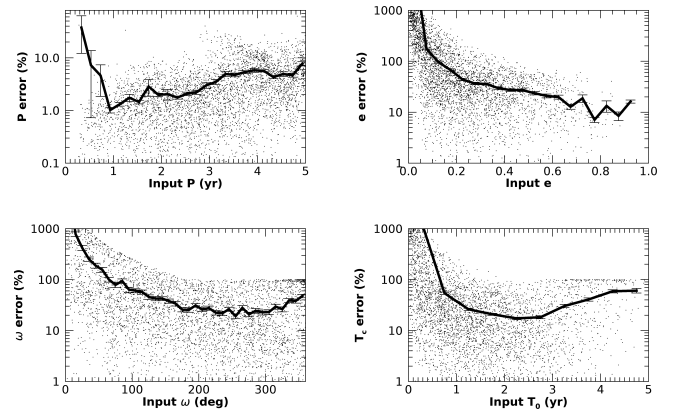


Figure 5. True errors on the relevant orbital parameters as a function of the input values, for the case of orbit determination with Gaia astrometry alone. Top left: orbital period; Top right: eccentricity; Bottom left: argument of periastron; Bottom right: epoch of periastron. In each panel, the thick solid lines correspond to the binned medians.

The main features of the dependence of the precision in period determination as a function of P itself were already described in e.g., Casertano et al. (2008) and Sozzetti et al. (2014). For example, Fig. 5 highlights how σ_P increases significantly both for $P \approx T$ as well as for short-period orbits which are under-sampled (as a direct effect of the scanning law) and translate in very low astrometric signals. On the other hand, well-sampled ($P < T$) orbital periods can be determined with $\sigma_P \sim 1 - 2\%$, particularly in the range $1.0 \lesssim P \lesssim 3.0$ yr. Similar behaviour is seen for σ_{T_0} , with an additional mild trend of improving precision with increasing eccentricity (plot not shown). The latter feature is expected as Fig. 5 also shows how σ_e decreases with increasing e , almost circular orbits having very large fractional uncertainties. As a consequence, σ_ω also decreases with increasing, better-determined values of e (plot not shown), and in general with increasing ω (Fig. 5).

Overall, the median values of the fractional errors on P , T_0 , e , and ω are $\mathbf{M}[\sigma_P] \sim 2\%$, $\mathbf{M}[\sigma_{T_0}] \sim 22\%$, $\mathbf{M}[\sigma_e] \sim 47\%$, and $\mathbf{M}[\sigma_\omega] \sim 26\%$, respectively. As expected, the quality of orbit determination also depends importantly on the astrometric signal-to-noise ratio. Casertano et al. (2008) and Sahlmann et al. (2015) had suggested thresholds of $S/N_{\text{ast},1} > 3$ and $S/N_{\text{ast},2} > 20$, respectively, for good astrometric orbit determination. The medians of the two diagnostics in our case are $\mathbf{M}[S/N_{\text{ast},1}] \sim 4$ and $\mathbf{M}[S/N_{\text{ast},2}] \sim 33$. We find that, specifically for edge-on orbit configurations, in order to improve the typical precision on the orbital parameters of interest one has to impose values of $S/N_{\text{ast},1}$ and $S/N_{\text{ast},2}$ significantly above the medians. For example, with $S/N_{\text{ast},1} > 10$ and $S/N_{\text{ast},2} > 60$, the median fractional uncertainties become $\mathbf{M}[\sigma_P] \sim 1\%$, $\mathbf{M}[\sigma_{T_0}] \sim 10\%$, $\mathbf{M}[\sigma_e] \sim 18\%$, and $\mathbf{M}[\sigma_\omega] \sim 11\%$, with fractional uncertainties thus reduced by a factor of 2 – 3. By further imposing $P < 3$ yr, we then obtain $\mathbf{M}[\sigma_P] \sim 0.3\%$, $\mathbf{M}[\sigma_{T_0}] \sim 6\%$, $\mathbf{M}[\sigma_e] \sim 18\%$, and $\mathbf{M}[\sigma_\omega] \sim 7\%$, with no further improvement in the typical precision in eccentricity determination. Finally, the median fractional uncertainties on i is $\mathbf{M}[\sigma_i] \approx 2.8\%$, a result already derived by Sozzetti et al. (2014). This number reduces to $\mathbf{M}[\sigma_i] \approx 0.9\%$, imposing the above mentioned thresholds on signal-to-noise ratio and orbital period.

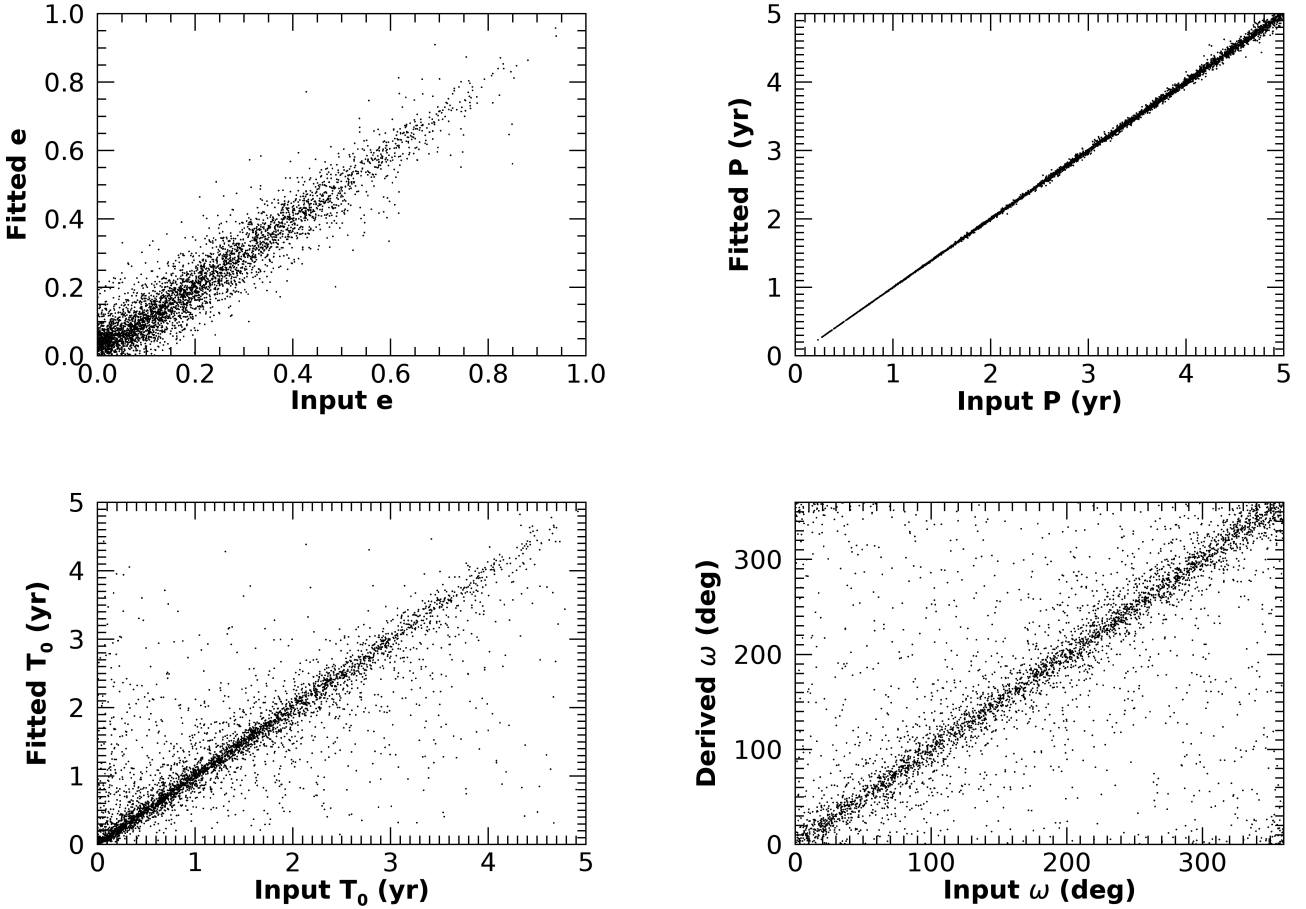


Figure 6. Fitted vs input value for the four orbital parameters relevant for the determination of the time of transit center in the combined astrometry+RV solutions. Top left: eccentricity; top right: orbital period; bottom left: epoch of periastron; bottom right: argument of periastron.

4.2 Astrometry only: Predicting the transit mid-time

The time of transit center T_c can be computed given P , T_0 , e and ω as follows (e.g., Irwin et al. 2008):

$$T_c = T_0 + \frac{P}{2\pi} (E - e \sin E), \quad (6)$$

where the eccentric anomaly $E = 2 \arctan[(1 - e)(1 + e)]^{1/2} \tan(\nu/2)$, and with the true anomaly at the time of central transit calculated as $\nu = \pi/2 - \omega$ for a perfectly edge-on orbit. The fractional uncertainty σ_{T_c} as a function of the input T_c value (Figure not shown) exhibits a clear similarity with the plot of σ_{T_0} vs T_0 , underlining the fact that the uncertainties in the determination P , e and ω play only a minor role in forecasting the time of transit center. Indeed, the median value $\mathbf{M}[\sigma_{T_c}] \sim 21\%$, virtually identical to that of σ_{T_0} . In units of days, the median uncertainty for the full sample is $\sigma_{T_c} \sim 97$ d. This number decreases by a factor ~ 2 if we consider either $P < 3$ yr or $S/N_{\text{ast},1} > 10$ ($S/N_{\text{ast},2} > 60$), while $\sigma_{T_c} \sim 20$ d in the case of the sub-sample satisfying both conditions simultaneously. The intrinsic $\pm\pi$ ambiguity in the determination of the argument of periastron when only astrometric measurements are available (Wright & Howard 2009) however implies that in practice two T_c values will need to be predicted, i.e. for $\omega + \nu = 90^\circ$ or 270° , with a corresponding doubled need of observing time investment for any follow-up programs probing the actual transiting nature of the detected companions (Perryman et al. 2014).

4.3 Combining Astrometry with Radial Velocities: orbit determination and transit mid-time forecast

As described in Sec.3, RV follow-up campaigns were simulated in case of a $\geq 5 - \sigma$ significance of the orbital semi-major axis. We focus here on quantifying the improvements in the determination of the orbital parameters directly affecting the forecast of the transit window. As is clearly seen in Fig. 6, there is a much tighter agreement between the fitted/derived values of P , e , T_0 and ω with respect to the astrometry-only case. The significant gain with the combined fits is quantified looking at the fractional error distributions for P , T_0 , e , and ω discussed in Sec. 4.1: these are significantly reduced, with median values $\mathbf{M}[\sigma_P] \sim 0.4\%$, $\mathbf{M}[\sigma_{T_0}] \sim 8\%$, $\mathbf{M}[\sigma_e] \sim 17\%$, and $\mathbf{M}[\sigma_\omega] \sim 8\%$, respectively. With the additional constraints on signal-to-noise ratio and orbital period discussed before, the above numbers become $\mathbf{M}[\sigma_P] \sim 0.1\%$, $\mathbf{M}[\sigma_{T_0}] \sim 3\%$, $\mathbf{M}[\sigma_e] \sim 7\%$, and $\mathbf{M}[\sigma_\omega] \sim 4\%$, respectively, with uncertainties reduced by factors 2.0–4.0. As expected, the quality of determination of the inclination angle is instead unaffected by the addition of RV measurements (at least for the illustrative examples of RV campaign utilized in this work), with median fractional errors essentially identical to the ones reported in the previous Section.

In terms of forecasting the time of transit center, the median value $\mathbf{M}[\sigma_{T_c}] \sim 8\%$, or ~ 34 d. This number decreases by factors of ~ 1.4 , ~ 2.3 and ~ 4.2 if we consider the sample with $S/N_{\text{ast},1} > 10$ ($S/N_{\text{ast},2} > 60$), $P < 3$ yr, and with both constraints applied, respectively.

Table 1. Median uncertainties on T_c based on orbit determination with Gaia astrometry alone and with the combined of Gaia astrometry and ground-based RVs observations.

Case	Astrometry only	Astrometry +RV
$\mathbf{M}[\sigma_{T_c}]$ (d), full sample	96.9	34.1
$\mathbf{M}[\sigma_{T_c}]$ (d), $S/N_{\text{ast},1} > 10$	47.3	24.3
$\mathbf{M}[\sigma_{T_c}]$ (d), $P < 3$ yr	45.6	14.7
$\mathbf{M}[\sigma_{T_c}]$ (d), $S/N_{\text{ast},1} > 10$ & $P < 3$	19.7	8.4

In the simplest case of a central transit and circular orbit, the transit duration is $t_d \approx 3 \text{ hr} \left(\frac{P}{4\text{d}}\right)^{1/3} \left(\frac{\varrho_\star}{\varrho_\odot}\right)^{-1/3}$ (Seager & Mallén-Ornelas 2003). For $P = 2$ yr and a typical $\varrho_\star \approx 5.5\varrho_\odot$ for the stellar sample under consideration here, then $t_d \approx 10$ hr. The uncertainty on the transit mid-time therefore remains the dominant factor even in the most favorable cases, with typical transit windows of $\sim \pm 2$ weeks at the $\sim 2\sigma$ level.

Finally, we also experimented doubling the amount of RV data within the same duration of the observing campaign. We recovered the expected improvement of a factor $\approx \sqrt{2}$ in the median precision with which P , e , T_0 , ω , and therefore T_c , were determined for the full sample.

5 SUMMARY AND DISCUSSION

In this paper we have gauged how the class of transiting cold Jupiters uncovered astrometrically by Gaia would benefit from the availability of additional Doppler measurements aimed at improving the accuracy of the orbital solutions and the corresponding transit ephemeris predictions for the purpose of confirming or ruling out the fact that the Gaia-detected companions do indeed transit. Our main findings can be summarized as follows:

- Based on realistic simulations of Gaia observations of systems composed of Jupiter-mass companions around a sample of nearby low-mass stars and state-of-the-art orbit fitting tools, we have shown how forecasts of the time of transit center will carry typical uncertainties of a few months, which might be reduced to about three weeks in the limit of very high astrometric signal-to-noise ratio and orbital periods < 3 yr;
- We have implemented a framework for combined astrometry+radial velocity orbital fits, and gauged the benefits of illustrative RV campaigns towards significant improvements in the identification of the possible transit windows, which will see typically reductions of the two figures above by a factor ~ 3 , with the added bonus of resolving the $\pm\pi$ ambiguity in the determination of the argument of periastron. A further summary of the key results is provided in Table 1.

Sozzetti et al. (2014), using the Besancon galaxy model of stellar populations (Robin et al. 2003) and reasonable assumptions for the frequency of giant planets within 3 au around M0-M9 dwarf primaries at $d \leq 100$ pc, estimated that, for fractional uncertainties on the inclination angle of 10%, 5% and 2%, Gaia alone could detect 255, 85 and 10 systems, respectively, formally compatible with transiting configurations within the 1σ error bars. Perryman et al. (2014) provided a figure of merit of ~ 650 detectable giant planets

with $1 < P < 10$ yr and $|\cos i| < 0.1$ around F-G-K-M dwarfs out to $\sim 400 - 500$ pc. The typical 2.5-yr RV follow-up campaign of transit candidates within $P \lesssim 5$ yr would entail an investment of ~ 0.5 observing nights per target at 4-m class facility equipped with a HARPS/HARPS-N like instrument. Monitoring of the top 100 candidates with the best constraints on orbital inclination would therefore require ~ 50 nights of observing time distributed over four observing semesters. This ballpark estimate indicates systematic RV follow-up campaigns of Gaia astrometrically detected candidate transiting gas giants are definitely feasible investing reasonable amounts of observing time. A potentially relevant caveat will however concern the achievement of the optimal balance in size of the candidate sample for follow-up based on updated expectations of false positive rates, which will better gauged when robust Gaia survey sensitivity estimates will become available.

In principle, follow-up photometric observations for confirmation of the transiting nature of the giant planetary companions could be carried out from the ground even with modest-size telescopes. However, while the transit depths ($\sim 1\%$) will have a magnitude readily accessible with ground-based facilities, the typical duration of the events will exceed that of a full observing night, requiring challenging multi-site campaigns for detection of partial events, such as the ones recently carried out to capture the transits of the long-period giant planets HD 80606 b (Pearson et al. 2022), HIP 41378 f (Bryant et al. 2021), and Kepler-167 e (Perrocheau et al. 2022), with orbital periods in the approximate range 100 – 1000 days². In addition, opportunities for follow-up from the ground will be very rare. As already suggested by Sozzetti et al. (2014) and Perryman et al. (2014), it might be beneficial to revisit photometric light-curve databases of long-term ground-based transit programs (e.g., SuperWASP, HATNet, HATSouth, MEarth, APACHE, etc.), looking for missed or uncategorized transit events in the time-series of the candidates (e.g., Cooke et al. 2018; Kovacs 2019; Yao et al. 2019, 2021). It will be however space-based transit photometry the likely most effective provider of confirmation/refutation measurements. Any candidates from Gaia in the original Kepler field would immediately benefit from the 4-yr long, continued Kepler photometry. The K2 mission and the TESS extended mission might also contribute to the task. Continuous, multi-year photometric monitoring of the fields that will ultimately be selected in the planned combination of long-duration observation and step-and-stare phases of the PLATO mission (Nascimbeni et al. 2022) will eventually be a crucial source of follow-up measurements of Gaia transiting planet candidates over a large fraction ($\sim 40\%$) of the observable sky. Our results reinforce the notion that Gaia astrometric detections of potentially transiting cold giant planets around bright stars, starting with Data Release 4, will constitute a valuable sample worthy of synergistic follow-up efforts with a variety of techniques, to identify those for which it might be possible in practice to perform spectroscopic characterization of their atmospheres.

ACKNOWLEDGEMENTS

This work has made use of data from the European Space Agency (ESA) mission *Gaia* (<https://www.cosmos.esa.int/>)

² Provided the primaries are bright and not slow rotators, a similar approach using multiple facilities for high-precision RV work can be implemented to follow-up long-period, lower-mass companions for the purpose of measurement of the Rossiter-McLaughlin effect, as it was successfully demonstrated recently in the case of HIP 41378 d (Grouffal et al. 2022).

gaia), processed by the *Gaia* Data Processing and Analysis Consortium (DPAC, <https://www.cosmos.esa.int/web/gaia/dpac/consortium>). Funding for the DPAC has been provided by national institutions, in particular the institutions participating in the *Gaia* Multilateral Agreement. We acknowledge financial contribution from the agreement ASI-INAF n.2018-16-HH.0. We gratefully acknowledge support from the Italian Space Agency (ASI) under contract 2018-24-HH.0 "The Italian participation to the *Gaia* Data Processing and Analysis Consortium (DPAC)" in collaboration with the Italian National Institute of Astrophysics.

DATA AVAILABILITY

The stellar data used in this study are available through the *Gaia* archive facility at ESA (<https://gea.esac.esa.int/archive/>) and the All-sky Catalog of Bright M dwarfs database (<https://vizier.cds.unistra.fr/viz-bin/VizieR-3?-source=J/AJ/142/138>). The synthetic data (simulation results) underlying this publication will be shared on reasonable request to the corresponding author.

REFERENCES

- Anders F., et al., 2022, *A&A*, **658**, A91
- Barnes J. R., Jeffers S. V., Jones H. R. A., 2011, *MNRAS*, **412**, 1599
- Beichman C., et al., 2014, *PASP*, **126**, 1134
- Beichman C. A., et al., 2018, *AJ*, **155**, 158
- Borucki W. J., et al., 2010, *Science*, **327**, 977
- Bryant E. M., et al., 2021, *MNRAS*, **504**, L45
- Casertano S., et al., 2008, *A&A*, **482**, 699
- Cooke B. F., Pollacco D., West R., McCormac J., Wheatley P. J., 2018, *A&A*, **619**, A175
- Cooke B. F., Pollacco D., Bayliss D., 2019, *A&A*, **631**, A83
- Cooke B. F., Pollacco D., Lendl M., Kuntzer T., Fortier A., 2020, *MNRAS*, **494**, 736
- Dalba P. A., Fulton B., Isaacson H., Kane S. R., Howard A. W., 2020, *AJ*, **160**, 149
- Dalba P. A., et al., 2021a, *AJ*, **161**, 103
- Dalba P. A., et al., 2021b, *AJ*, **162**, 154
- Dalba P. A., et al., 2022, *AJ*, **163**, 61
- Dholakia S., Dholakia S., Mayo A. W., Dressing C. D., 2020, *AJ*, **159**, 93
- Drimmel R., Sozzetti A., Schröder K.-P., Bastian U., Pinamonti M., Jack D., Hernández Huerta M. A., 2021, *MNRAS*, **502**, 328
- Eastman J., Gaudi B. S., Agol E., 2013, *PASP*, **125**, 83
- Eriksson U., Lindegren L., 2007, *A&A*, **476**, 1389
- Foreman-Mackey D., Morton T. D., Hogg D. W., Agol E., Schölkopf B., 2016, *AJ*, **152**, 206
- Gaia* Collaboration et al., 2016, *A&A*, **595**, A1
- Gaia* Collaboration et al., 2022a, arXiv e-prints, p. arXiv:2206.05595
- Gaia* Collaboration et al., 2022b, arXiv e-prints, p. arXiv:2208.00211
- Giles H. A. C., et al., 2018, *A&A*, **615**, L13
- Gill S., et al., 2020, *MNRAS*, **495**, 2713
- Grouffal S., et al., 2022, arXiv e-prints, p. arXiv:2210.14125
- Halbwachs J.-L., et al., 2022, arXiv e-prints, p. arXiv:2206.05726
- Hébrard G., et al., 2019, *A&A*, **623**, A104
- Herman M. K., Zhu W., Wu Y., 2019, *AJ*, **157**, 248
- Holl B., et al., 2022, arXiv e-prints, p. arXiv:2206.05439
- Irwin J., et al., 2008, *ApJ*, **681**, 636
- Kipping D. M., 2013, *MNRAS*, **434**, L51
- Kovacs G., 2019, *A&A*, **625**, A145
- Kunimoto M., Winn J., Ricker G. R., Vanderspek R. K., 2022, *AJ*, **163**, 290
- LaCourse D. M., Jacobs T. L., 2018, *Research Notes of the American Astronomical Society*, **2**, 28
- Lattanzi M. G., Spagna A., Sozzetti A., Casertano S., 2000, *MNRAS*, **317**, 211
- Lépine S., Gaidos E., 2011, *AJ*, **142**, 138
- Lindegren L., et al., 2021, *A&A*, **649**, A2
- Makarov V. V., Beichman C. A., Catanzarite J. H., Fischer D. A., Lebreton J., Malbet F., Shao M., 2009, *ApJ*, **707**, L73
- Meunier N., Lagrange A. M., 2022, *A&A*, **659**, A104
- Meunier N., Lagrange A. M., Borgniet S., 2020, *A&A*, **644**, A77
- Nascimbeni V., et al., 2022, *A&A*, **658**, A31
- Osborn H. P., et al., 2016, *MNRAS*, **457**, 2273
- Pearson K. A., et al., 2022, *AJ*, **164**, 178
- Perrocheau A., et al., 2022, arXiv e-prints, p. arXiv:2211.01532
- Perryman M., Hartman J., Bakos G. Á., Lindegren L., 2014, *ApJ*, **797**, 14
- Robin A. C., Reylé C., Derrière S., Picaud S., 2003, *A&A*, **409**, 523
- Sahlmann J., Triaud A. H. M. J., Martin D. V., 2015, *MNRAS*, **447**, 287
- Seager S., Mallén-Ornelas G., 2003, *ApJ*, **585**, 1038
- Sowmya K., Nèmec N. E., Shapiro A. I., Işık E., Witzke V., Mints A., Krivova N. A., Solanki S. K., 2021, *ApJ*, **919**, 94
- Sozzetti A., 2005, *PASP*, **117**, 1021
- Sozzetti A., Giacobbe P., Lattanzi M. G., Micela G., Morbidelli R., Tinetti G., 2014, *MNRAS*, **437**, 497
- Ter Braak C. J. F., 2006, *Statistics and Computing*, **16**, 239
- Uehara S., Kawahara H., Masuda K., Yamada S., Aizawa M., 2016, *ApJ*, **822**, 2
- Ulmer-Moll S., et al., 2022, *A&A*, **666**, A46
- Villanueva Steven J., Dragomir D., Gaudi B. S., 2019, *AJ*, **157**, 84
- Wang J., et al., 2015, *ApJ*, **815**, 127
- Wright J. T., Howard A. W., 2009, *ApJS*, **182**, 205
- Yao X., et al., 2019, *AJ*, **157**, 37
- Yao X., et al., 2021, *AJ*, **161**, 124

This paper has been typeset from a $\text{\TeX}/\text{\LaTeX}$ file prepared by the author.